HEALTH AND MEDICINE

Magnetic soft robotic bladder for assisted urination

Youzhou Yang[1,2]†, Jiaxin Wang[1,3]†, Liu Wang[4]†, Qingyang Wu[2]†, Le Ling[1,3], Yueying Yang[2], Shan Ning[2], Yan Xie[5,6], Quanliang Cao[5,6], Liang Li[5,6], Jihong Liu[1,3]*, Qing Ling[1,3]*, Jianfeng Zang[2,7]*

The poor contractility of the detrusor muscle in underactive bladders (UABs) fails to increase the pressure inside the UAB, leading to strenuous and incomplete urination. However, existing therapeutic strategies by modulating/repairing detrusor muscles, e.g., neurostimulation and regenerative medicine, still have low efficacy and/or adverse effects. Here, we present an implantable magnetic soft robotic bladder (MRB) that can directly apply mechanical compression to the UAB to assist urination. Composed of a biocompatible elastomer composite with optimized magnetic domains, the MRB enables on-demand contraction of the UAB when actuated by magnetic fields. A representative MRB for a UAB in a porcine model is demonstrated, and MRB-assisted urination is validated by in situ computed tomography imaging after 14-day implantation. The urodynamic tests show a series of successful urination with a high pressure increase and fast urine flow. Our work paves the way for developing MRB to assist urination for humans with UABs.

INTRODUCTION

Voluntary urination requires the contraction of the detrusor muscle to increase the pressure inside the bladder by a threshold, a.k.a. detrusor pressure (denoted as ΔP) (1, 2). Detrusor pressure is usually calculated by subtracting abdominal pressure (P_{abd}) from bladder pressure P_{ves}, i.e., $\Delta P = P_{ves} - P_{abd}$. For example, ΔP needs to achieve 30 to 40 cmH$_2$O (1 cmH$_2$O $\approx$ 98.07 Pa and 40 cmH$_2$O $\approx$ 3.92 kPa) for humans to urinate (3, 4) (Fig. 1A). Reduced contractility of the detrusor muscle usually leads to an underactive bladder (UAB) with numerous urination problems such as prolonged and incomplete voiding (Fig. 1B) (5–7). UAB has been a strenuous life challenge with various health care implications, e.g., bilateral hydronephrosis, pyelectasis, and renal failure (8, 9), which afflicts 9 to 48% of men and 12 to 45% of elderly women (10–12).

Now, because of the low and/or side effects of the clinic oral drugs (13), most patients with UABs have to adopt intermittent self-catheterization for uncontrollable urination (14, 15). However, such a catheterization process often incurs infections, not to mention the extreme inconvenience when performed multiple times daily. Recent clinical trials attempt to treat UAB by modulating/repairing detrusor muscles via electrical nerve stimulation (16–18) and regenerative medicines (19). Typical examples include intravesical electrotherapy (20), transcutaneous electrotherapy (21), and stem cell injection (22). However, because of the hard-to-reverse nerve damage/loss and

elusive target regulation, these therapeutic strategies have limited efficacy and thus have not been adopted in routine treatment (see table S1) (16, 23, 24).

Recently, to achieve a voluntary, continuous, and complete urination, directly pressurizing the UAB by mechanical forces has been proposed as an alternative strategy that holds great promise in assisting urination (25). For example, Hassani et al. (26–29) developed a shape memory alloy–based artificial bladder that can compress the UAB in a mouse when heated by electricity. Yang et al. (30) presented a thermoresponsive hydrogel bladder that can apply compressive forces to the UAB upon heating. These seminal works, however, only show a limited pressure increase in the UAB (i.e., ΔP is low) and have not been systematically validated by in vivo urodynamic tests (31). In addition, the actuation of the abovementioned artificial bladders relies on the temperature change, which usually takes quite a long time. Therefore, developing an artificial bladder that can achieve on-demand contraction of UAB with a high pressure increase in the bladder (i.e., ΔP is high) is of great significance, yet has not been demonstrated and validated.

Here, we propose a strategy of building an implantable artificial bladder—magnetic soft robotic bladder (MRB)—that can promptly apply a high compressive force to the UAB to assist urination via magnetic actuation (Fig. 1C). The MRB is composed of pure silicone and magnetic composites, i.e., hard magnetic microparticles dispersed in the silicone matrix (Fig. 1D). The compressive force is rapidly imparted by the magnetic attraction between dispersed hard magnetic microparticles and the actuation magnetic field. The MRB is rationally designed by optimizing both magnetomechanical properties and patterns of magnetic composites to achieve a high compressive force and a low weight for long-term implantation. We demonstrate a representative MRB in a UAB porcine model and validate the assisted urination by in situ computed tomography (CT) imaging after 14-day implantation. In addition, the urodynamic tests show a pressure increase in the UAB greater than 37 cmH$_2$O, followed by a series of successful urination without retention. Given the similarity in both bladder shape and urodynamics between porcine and humans, our work can pave the way for developing MRB to assist urination for humans with UABs (Fig. 1E).

[1]Department of Urology, Tongji Hospital, Tongji Medical College, Huazhong University of Science and Technology, Wuhan 430030, PR China. [2]School of Optical and Electronic Information and Wuhan National Laboratory for Optoelectronics, Huazhong University of Science and Technology, Wuhan 430074, PR China. [3]Institute of Urology, Tongji Hospital, Tongji Medical College, Huazhong University of Science and Technology, Wuhan 430030, PR China. [4]CAS Key Laboratory of Mechanical Behavior and Design of Materials, Department of Modern Mechanics, University of Science and Technology of China, Hefei 230026, PR China. [5]Wuhan National High Magnetic Field Center, Huazhong University of Science and Technology, Wuhan 430074, PR China. [6]State Key Laboratory of Advanced Electromagnetic Engineering and Technology, Huazhong University of Science and Technology, Wuhan 430074, PR China. [7]The State Key Laboratory of Digital Manufacturing Equipment and Technology, Huazhong University of Science and Technology, Wuhan 430074, PR China.
*Corresponding author. Email: jfzang@hust.edu.cn (J.Z.); lingqing@tjh.tjmu.edu.cn (Q.L.); jhliu@tjh.tjmu.edu.cn (J.L.)
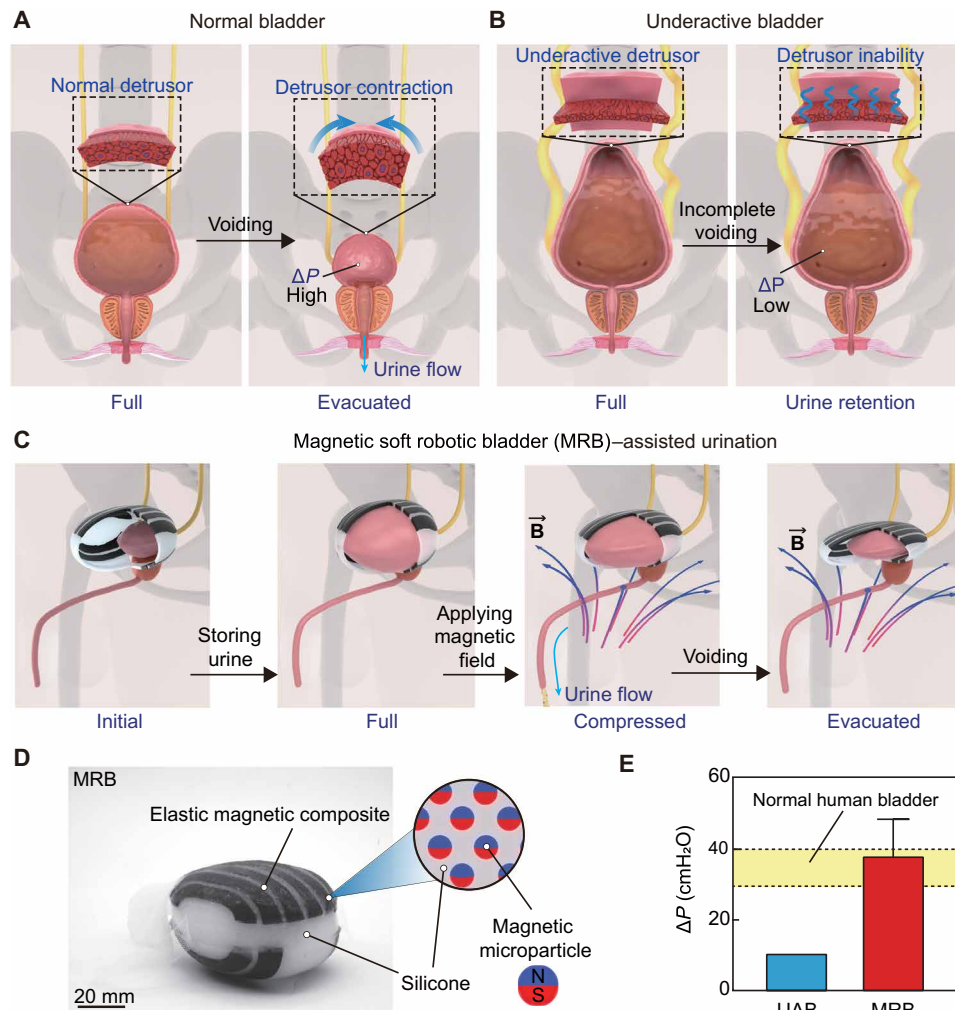†These authors contributed equally to this work.

Fig. 1. MRB for assisted urination of a UAB. (**A**) Schematic of the complete voiding process of a normal bladder. The detrusor contracts the bladder at the full state and increases the pressure inside the bladder, denoted as ΔP. (**B**) A UAB (often in a Christmas tree shape) is characterized by underactive detrusor muscles with reduced ΔP and incomplete voiding with urine retention. (**C**) Schematic illustration of MRB-assisted urination. (**D**) The MRB is composed of pure silicone and magnetic composites, i.e., hard magnetic microparticles dispersed in the silicone matrix. N and S denote as north and south pole of magnet microparticle, respectively. (**E**) MRB can increase the pressure inside the UAB by 30 to 40 cmH$_2$O, which is comparable to the required value for voluntary urination of a normal bladder in humans.

RESULTS

Rational design of MRB

Three rationales are considered in designing an implantable MRB. First, the three-dimensional (3D) geometry of the MRB should match that of the UAB at the full state so that the MRB does not affect urine storage (Fig. 1C). Second, the MRB should apply high compressive force (i.e., pressure increase ΔP is high) to assist urination upon magnetic actuation. Third, the MRB should have a lightweight (denoted as W) for long-term implantation. The optimal design can be found by model-guided optimization of the magnetomechanical properties and patterns of the magnetic composite.

Here, we select a porcine bladder as a representative model to demonstrate our design strategy due to the similarity in bladder shape, capacity, and urodynamics between porcine and humans (e.g., pressure increase for urination ΔP of 30 to 40 cmH$_2$O) (*3, 4, 32*). We first build the 3D model of the MRB by reconstructing the bladder at its full state (fig. S1). The elastomer magnetic composite is made

by dispersing neodymium-iron-boron (NdFeB) microparticles (average size ~5 μm) in a silicone matrix (shear modulus ~24 kPa; Ecoflex, Smooth-On Inc.). By changing the NdFeB microparticle volume fraction from 15 to 40%, the magnetization (denoted as **M**), density, and shear modulus of the magnetic composite can be effectively tuned from 81 to 225 kA/m, 2 to 3.64 g/m^3, and 80 to 550 kPa, respectively (fig. S2). As illustrated in Fig. 2A, we propose four magnetic patterns: top surface fully covered by magnetic composites (pattern A), both top and bottom surface fully covered by magnetic composites (pattern B), seven composite strips on the top surface (pattern C), and seven composite strips on the top surface and four strips on the bottom surface (pattern D). Each pattern has six different NdFeB volume fractions (i.e., volume % = 15, 20, 25, 30, 35, and 40%). In total, we have 24 designs of MRB. Note that composite with NdFeB volume fraction larger than 40% may not be feasible due to the close packing of microparticles (*33–35*).

The driving force for compressing the MRB originates from the magnetic attraction between dispersed NdFeB microparticles and
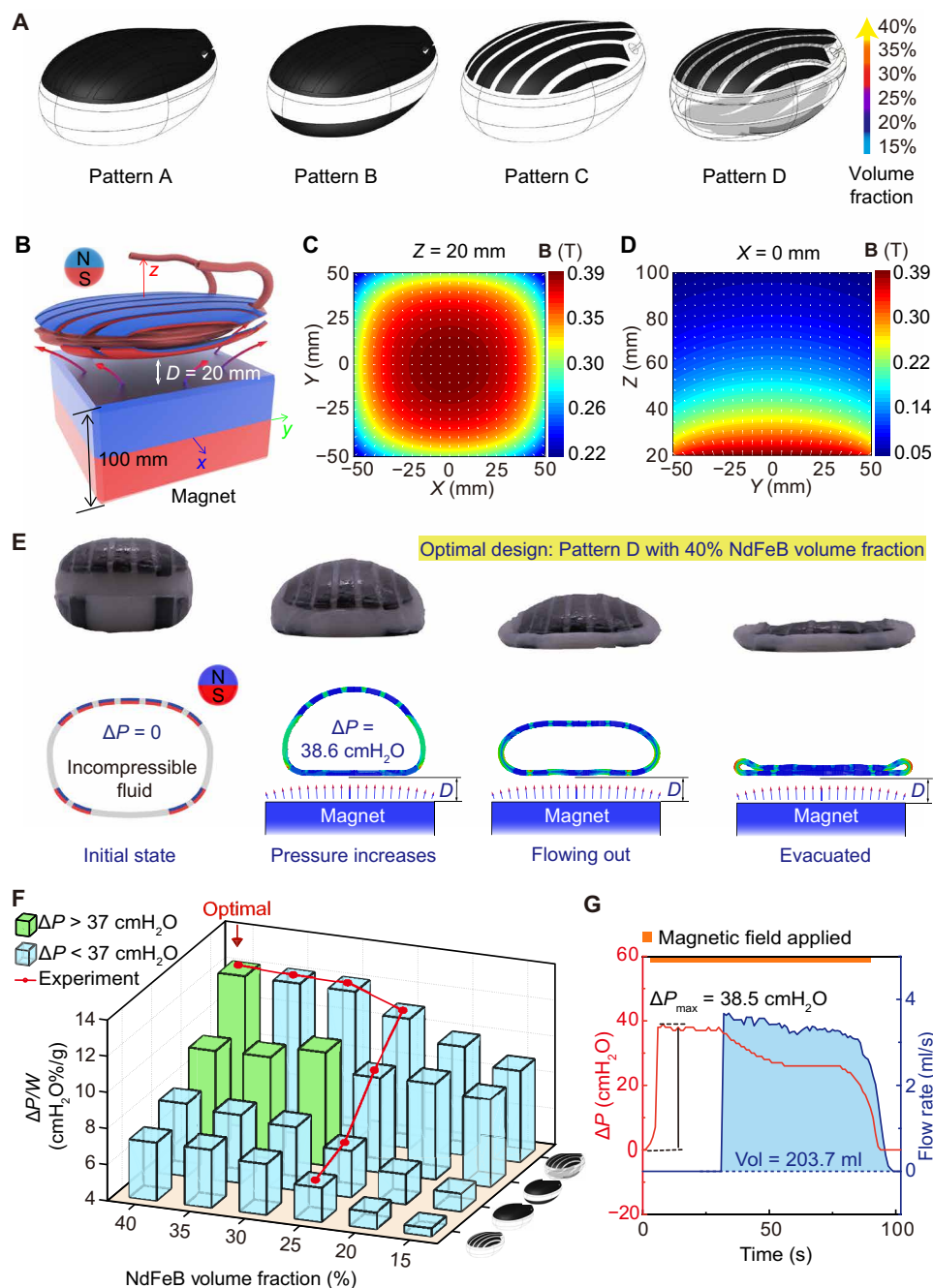
Fig. 2. Model-guided design, optimization, and experimental validation of MRB. (**A**) Illustration of four magnetic patterns: top surface fully covered by magnetic composites (pattern A), both top and bottom surface fully covered by magnetic composites (pattern B), seven composite strips on the top surface (pattern C), and seven composite strips on the top surface and four strips on the bottom surface (pattern D). Each pattern has six NdFeB volume fractions (15, 20, 25, 30, 35, and 40%). (**B** to **D**) Magnetic flux direction and density distributions on an XY plane at $Z = 20$ mm and a YZ plane at $X = 0$ mm produced by a cubic magnet (NdFeB, n52, width 10 cm, residual magnetic flux density $\mathbf{B}_r = 1.4$ T). (**E**) Experimental and finite element simulation results in the deformation of the optimized MRB in magnetic-assisted urination. The minimal distance between MRB and magnet (denoted as D) is 20 mm. (**F**) Simulated and experimental results of the maximum normalized pressure increase $\Delta P/W$ of 24 MRBs. MRBs that achieve $\Delta P > 37$ cmH$_2$O are labeled with green, while others are labeled with blue. (**G**) Ex vivo experimental results of the urodynamic test of the optimized MRB.

the actuation magnetic field, which includes both a magnetic torque density $\boldsymbol{\tau} = \mathbf{M} \times \mathbf{B}$ and a body force $\mathbf{f} = (\mathbf{M} \cdot \nabla)\mathbf{B}$, where $\mathbf{B}$ and $\nabla\mathbf{B}$ represent the magnetic flux density and the gradient of the magnetic field, respectively (*36*, *37*). Here, we adopt a cubic magnet (NdFeB,

n52, width 10 cm, residual magnetic flux density $\mathbf{B}_r = 1.4$ T; Fig. 2B) as a representative source of the magnetic field. The magnetic fields and gradients are shown in Fig. 2(C and D) and fig. S3. The primary reasons for choosing such a magnet (rather than electromagnetic

coils) are twofold (38, 39). First, it can provide high magnetic field strength in a large free space. Second, in the absence of high-current electricity, it offers ease of operation and safety.

Finite element (FE) simulations are carried out to analyze the contraction capability of MRBs upon magnetic actuation (Fig. 2E, fig. S4, and movie S1). By using the "Fluid Cavity" function in Abaqus, the MRB is initially modeled as a 3D cavity fully filled with incompressible fluid to emulate the full UAB after storing the urine. By moving the cubic magnet to the MRB, the MRB contracts. During this process, the volume of the MRB is assumed to be constant due to the filled incompressible fluid. Therefore, the contraction of MRB increases the hydraulic pressure of the fluid, i.e., the simulated detrusor pressure ΔP increases. The minimum actuation distance (denoted as D in Fig. 2E) is set to be 2 cm (close to the thickness of the belly fat) (40), at which the maximum ΔP is recorded. Thereafter, the volume constraint of the cavity is deactivated, and MRB further contracts to simulate the urine flowing out until empty. To achieve a high contraction capability and lightweight, we determine the optimal MRB to have the largest $\Delta P/W$ while satisfying $\Delta P > 37$ cmH$_2$O. Note that $\Delta P = 37$ cmH$_2$O is a relatively high value that usually can guarantee a successful urination in humans. Results of $\Delta P/W$ of 24 MRBs are plotted in Fig. 2F in which the green and blue bars represent MRBs with $\Delta P > 37$ cmH$_2$O and $\Delta P < 37$ cmH$_2$O, respectively. Figure 2F shows that the optimal MRB is pattern D with 40% NdFeB volume fraction, which corresponds to $\Delta P = 38.6$ cmH$_2$O (3.78 kPa) and $W = 313.5$ g (fig. S5). The simulated urination process of the optimal MRB is plotted in Fig. 2E. It is worth noting that adding magnetic composites to the bottom surface plays a critical role in increasing the pressure. This is because, in addition to the compression of the top surface, magnetic composite on the bottom surface further stretches the MRB when actuated (fig. S4), elevating the hydraulic pressure in the fluid because of the incompressibility constraint. To validate FE simulation results, seven different MRBs including the optimal design are fabricated by a multistep cast process based on Ecoflex, a widely used biocompatible silicone (fig. S6), and their maximum ΔP is tested (fig. S7). Experimental results are plotted by the red line in Fig. 2F and agree excellently with FE simulation results. In particular, for the optimal design, $\Delta P = 38.5$ cmH$_2$O is measured, a consistent flow with a total volume of 203.7 ml is observed (Fig. 2G and movie S2), and the maximum ΔP is only measured when MRB is parallel to the magnet (fig. S8). Such a voiding behavior is comparable to the performance of a normal human bladder, which demonstrates the potential applications for treating UABs in humans. Note that the stiffness of the nonmagnetized soft body of MRB is also investigated. We show that, when the shear modulus of the soft body is tuned from 24 to 150 kPa, the maximum pressure ΔP is almost the same (fig. S9). Also, FE simulations without considering magnetic field gradients (fig. S3) show that the maximum ΔP is only 9.53 cmH$_2$O (0.94 kPa), suggesting that the major contribution to contracting the MRB is the magnetic body forces (fig. S10).

Implantation feasibilities of MRB
In addition to the assisted urination function, we also consider the long-term implantation feasibilities of MRB that mainly include in-body fixations, biocompatibility, and repeatability. As has been proven a safe material for long-term implantation (41), a titanized polypropylene mesh is used to bind the MRB with pelvic fascia (Fig. 3A). To fix the MRB as a cover of the UAB, two holes at the posterior are reserved for ureters, preserving an unobstructed urine

tract. A neck sheath is then used to wrap up the urethra to prevent the bladder from sliding out of the MRB. Notably, the MRB is not directly sutured to the UAB or urethral tissue to prevent any interfacial stress between them. Also, these fixations exert negligible resistance to the UAB during urine storage. As evidenced by the experimental data in Fig. 3B, the pressure increase in the UAB with and without MRB is almost the same when the UAB is infused with 300 ml of saline. The minimal influence of the implanted MRB on the internal organs is also validated by an ex vivo test (fig. S11).

To enhance biocompatibility, the surfaces of MRB are coated with a thin layer (~18 μm) of polyacrylamide, so-called hydrogel skin (Fig. 3A and fig. S12) that has been reported by several pioneer works (42–44). As also validated in our experiment (Fig. 3C and fig. S12), the hydrogel skin can significantly reduce contact friction between the MRB and the internal organs. The hydrogel skin also reduces the toxicity of the MRB, according to the ex vivo test on bladder epithelium cells (Fig. 3D and fig. S12, D and E). It is also worth noting that the hydrogel skin can be directly coated on the silicone (Ecoflex) surface. However, because the surface of the magnetic composite is a bit rough, a thin interface layer of Ecoflex (~20 μm) is first coated before coating the hydrogel.

Another key aspect of long-term implantation is repeatability. We continuously test the MRB for over 20,000 s by first filling it with water and then compressing the MRB using the cubic magnet (Fig. 3E). In total, 1000 cycles are tested to mimic the urine storage and MRB-assisted urination over half a year based on the average of five to six times of daily urination for humans (2). As shown in Fig. 3E and fig. S13, pressure increase $\Delta P > 37$ cmH$_2$O and almost complete voiding behavior are observed after 1000 cycles. Also, the MRB still preserves an excellent shape without noticeable failure in both material and structure, demonstrating excellent repeatability.

UAB porcine model validation
To validate the optimized MRB in vivo, we construct a UAB porcine model and test MRB-assisted urodynamics after 14-day implantation. To construct the UAB model, we first transect the S2 to S4 nerves of the porcine to denervate its voluntary urination (fig. S14, A to C). By doing this, both bladder sphincter and detrusor are in a relatively relaxed state, which avoids the closure of the sphincter when the bladder contracts and prevents the reflux of urine to the upper urinary tract. The detached S2-S4 nerves are confirmed by the magnetic resonance images before and 7 days after surgery (fig. S14, D and E). To verify the constructed UAB model, we first perform urodynamic tests of the UAB without MRB (fig. S14, F and G). In contrast to the normal bladder that can voluntarily urinate when infused with saline up to 330 ml (fig. S14, H and I), the UAB cannot trigger urination despite that the pressure inside the UAB can slightly increase when infused with saline up to 700 ml (fig. S14J), manifesting that a successful UAB model is constructed.

Thereafter, the MRB is implanted on the UAB via a surgery procedure inspired by female pelvic floor reconstruction (Fig. 4A) (45). First, the skin and abdominal wall are incised successively, and the UAB is then completely isolated (fig. S15, A and B). Second, the sheath of MRB is wrapped around the urethra of the porcine and sutured for immobilization (fig. S15, C and D). Two pairs of titanized meshes that extend from the bottom of the MRB are threaded through the obturator foramen and are drawn to the skin for fixation by a special hook (fig. S15E). Another pair of meshes extending from the lateral wall is passed through the iliac muscle and skin to complete the fixation and implantation process (Fig. 4B and fig. S15, F to H).
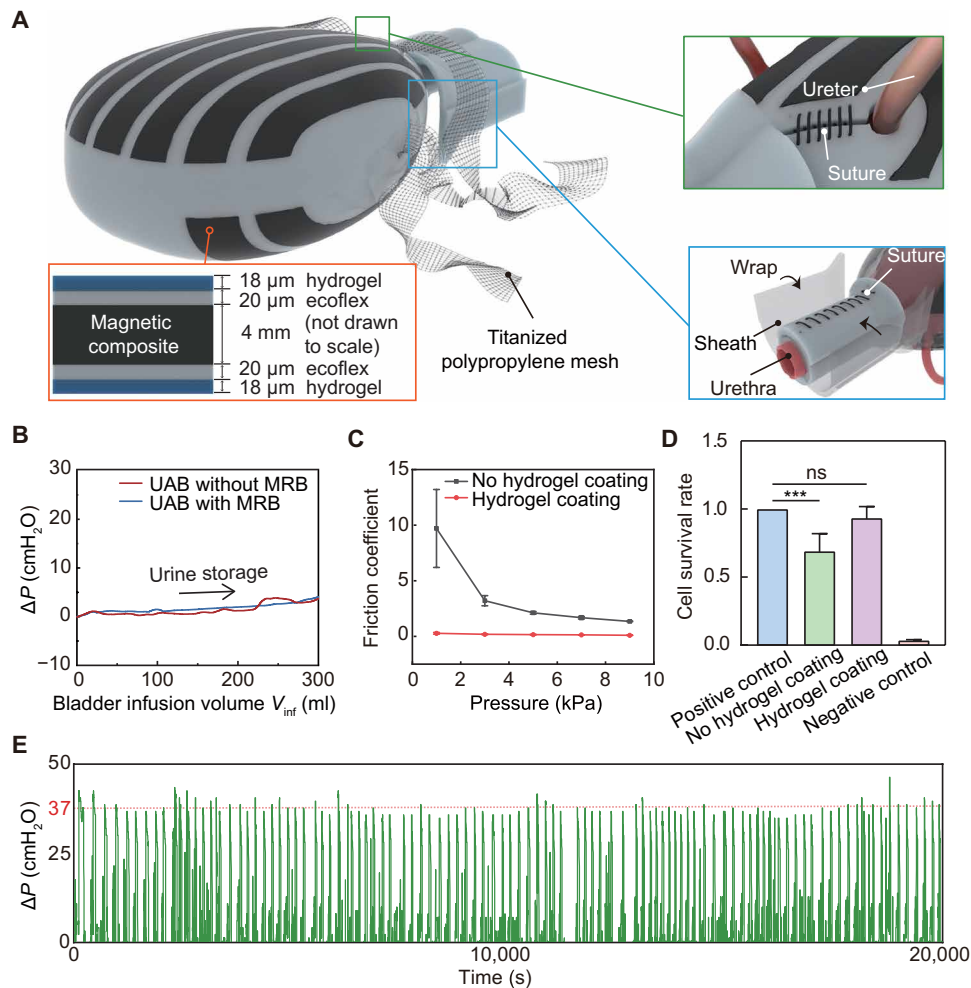
Fig. 3. Implantation feasibility (fixation, biocompatibility, and repeatability) of MRB. (**A**) A titanized polypropylene mesh is used to bind the MRB with pelvic fascia. Two holes at the posterior are reserved for ureters (green box). A neck sheath is used to wrap up the urethra to prevent the bladder from sliding out of the MRB (blue box). The cross-sectional view of the magnetic composite shows that the MRB is coated with a thin layer of hydrogel (~18 μm) (orange box). (**B**) Comparison of pressure increase ΔP during the urine storage for UABs with and without MRB. (**C**) Comparison of the friction coefficient of magnetic composites with and without hydrogel coating. (**D**) Toxicity test of the MRB. No statistical difference (ns) is observed between the positive control (culture medium only) and MRB with hydrogel coating. ***$P < 0.05$. (**E**) Measurement of the pressure increase ΔP inside the UAB in 20,000 s by cyclicly filling the UAB and MRB-assisted voiding, which corresponds to 1000 cycles of simulated urination.

To verify the implantation and demonstrate the MRB-assisted urination, we first conduct CT and video urodynamics of the MRB on postoperative day (POD) 14 (Fig. 4C and movie S3). The contour of the implanted MRB is extracted from a high-density shadow that surrounded the bladder in the CT image (the outline of the bladder was denoted with a dotted line). The CT images on reference planes indicate that the MRB is properly implanted and fixed without interfering with surrounding tissues. In the video urodynamic test, 330 ml of saline with a contrast agent (relatively high-density shadow in CT imaging) is injected into the bladder. When the cubic magnet is moved to the MRB, the in situ CT imaging results show that the MRB can rapidly compress the UAB upon magnetic actuation (Fig. 4C), suggesting that MRB-assisted urination can be voluntarily controlled. The representative urodynamic wave pattern with pressure increase inside the UAB $\Delta P = 38.4$ cmH$_2$O is observed (Fig. 4D), which is similar to that of a normal bladder (fig. S14H). The urine can be observed flowing out of the external urethral orifice. For consideration of the operator's

safety in the radiation environment, the video urodynamic test is only performed the 20 s. Within such a short period of time, 110 ml of urine is already excreted, leading to a significantly reduced volume of the UAB as confirmed by the 3D reconstruction from CT images (Fig. 4E). It is also worth noting that no urine reflux enters the ureter during MRB-assisted urination (fig. S16, A and B), indicating that MRB-assisted urination did not surpass the pressure of the urethral sphincter.

To further evaluate the MRB-assisted urination, multiple urodynamic tests are performed on POD 7 and 14 (fig. S16E). Results in Fig. 5A show a successful urination performance in four cycles of infusion (260 ml) and voiding (movie S4). As evidenced in Fig. 5B, the maximum pressure increase inside the UAB can still achieve $\Delta P = 37.2$ cmH$_2$O (3.65 kPa) and 225 ml of urine is discharged at a flow rate of 18.9 ml/s, suggesting almost a complete voiding within 55 s. The average pressure increase on POD 7 and 14 can reach $\Delta P = 40.90 \pm 11.62$ cmH$_2$O and 35.55 ± 6.04 cmH$_2$O, respectively (Fig. 5C and fig. S16, C and D).
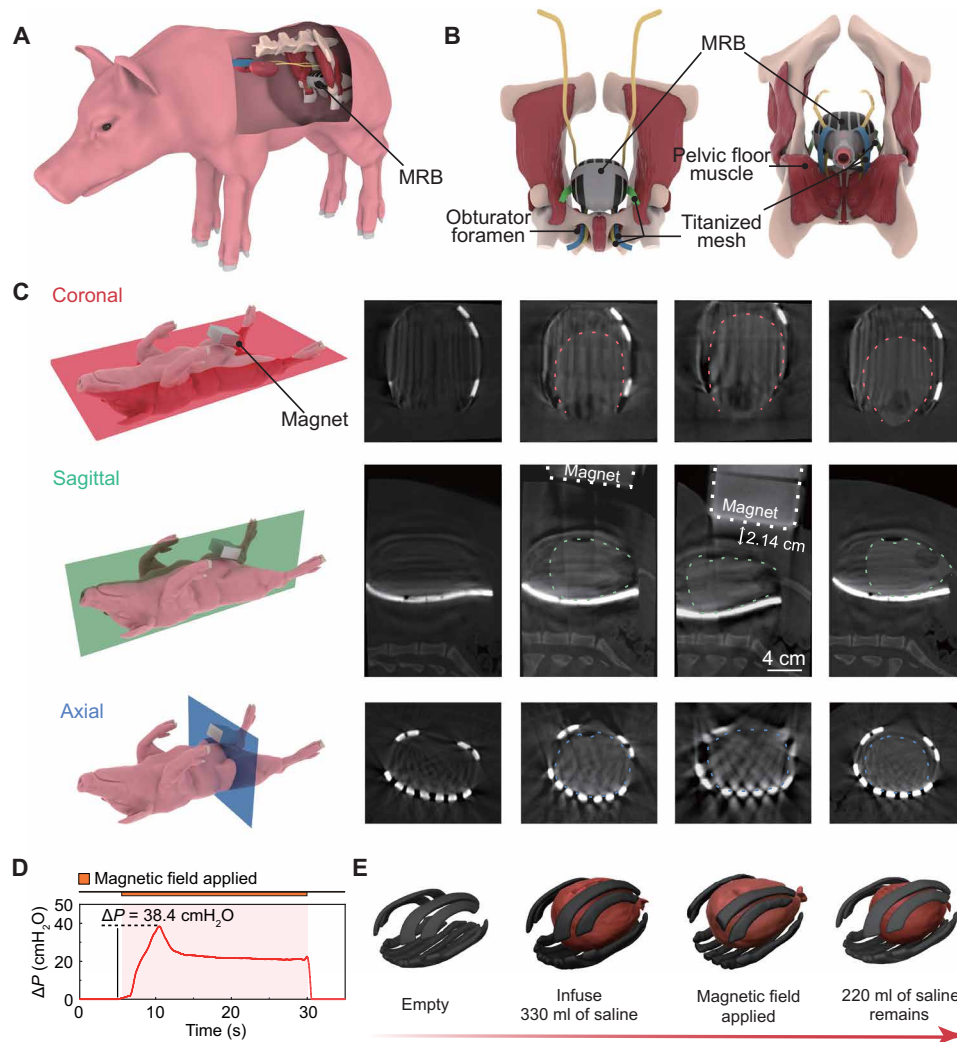
Fig. 4. In vivo CT images of the MRB-assisted urination of a UAB porcine model after 14-day implantation. (**A**) Schematic of the implanted MRB in a UAB porcine model. (**B**) Anatomical diagram of MRB fixation. (**C**) In vivo video urodynamic images of the implanted MRB. From left to right, four columns represent different states of assisted urination: empty state, infusion with saline, the magnetic field applied, and after compression. The dashed lines indicate the bladder boundary. The minimal actuation distance is measured as 2.14 cm. (**D**) Corresponding pressure increase ΔP during the video urodynamic test. (**E**) 3D reconstructed model of the UAB and magnetic composites from corresponding columns of the image in (C).

To verify the long-term biocompatibility of the implanted MRB, the blood parameters, urine parameters, and renal function are also evaluated on POD 3, 7, and 14. Results indicate that implantation of the MRB has no substantial influence on blood parameters and renal function (fig. S16, F and H). We note that the number of white blood cells in the urine increases over time (fig. S16G). However, such an infection may be due to daily catheterization to prevent urinary retention. In addition, similar behavior scores are obtained between preoperative and postoperative behavior analysis, suggesting that implantation does not affect the routine activities of the porcine (fig. S16I and table S2). The histology after the pigs are euthanized shows that, except for a small amount of inflammation in the bladder serosal layer directly in contact with the MRB, there is no obvious inflammatory cell infiltration in the bladder mucosa and urethra (Fig. 5D and fig. S17A to F). Moreover, no dilations are observed in the ureters and kidneys, indicating that no urinary reflux occurred (Fig. 5E and fig. S17B). Immunohistochemical staining of interleukin 6 (IL-6)

further confirms the results of hematoxylin and eosin (H&E) staining (fig. S17, G to J).

DISCUSSION

Conventional methods such as modulating/repairing detrusor muscles still face obstacles in treating patients with UABs, especially for those with damaged nerves. Distinctly, we propose a novel strategy of constructing artificial bladders—MRB that can directly compress the UAB to urinate. By using magnetically responsive soft materials, the MRB can achieve on-demand urination upon magnetic actuation. The MRB is optimized by model-based simulations to achieve both high compression capability for assisted urination and low weight for long-term implantation.

The implantation biocompatibility and efficacy of the MRB are validated in a UAB porcine model. First, MRB is coated with a thin layer of hydrogel to markedly reduce its friction and toxicity. Second,
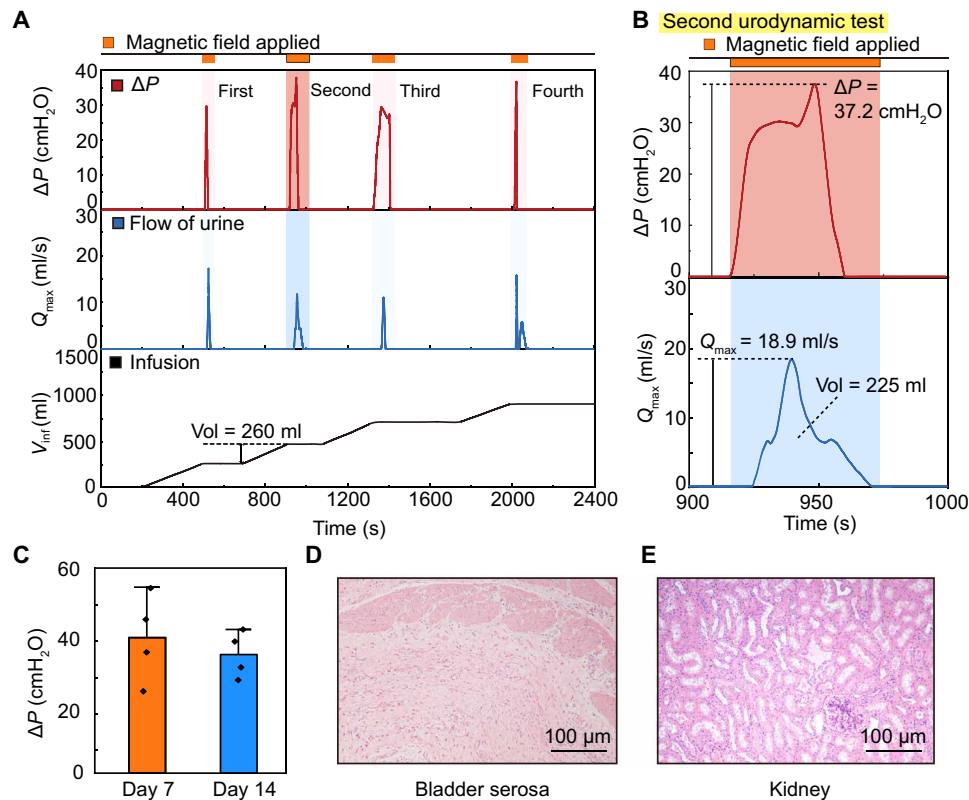
Fig. 5. In vivo urodynamic characterization and long-term biocompatibility of a UAB porcine model implanted with MRB. (**A**) Representative urodynamic curves of ΔP, maximum urine flow rate (Q_{max}), and bladder infusion volume (V_{inf}) as a function of time during four cycles of MRB-assisted voiding process. (**B**) Magnified view of ΔP and Q_{max} of the second urodynamic test in (A). (**C**) Pressure increase ΔP on POD 7 and 14. (**D** and **E**) Hematoxylin and eosin staining of porcine bladder serosa and kidney, respectively.

a set of titanized polypropylene meshes are used to fix the MRB inside the body as confirmed by the CT images after 14-day implantation. Last, the MRB can effectively enhance the pressure inside the UAB that successfully triggers a series of urination when actuated by a magnetic field. MRB-assisted urination is validated by both CT images and urodynamic characterization. Given the similarity in shapes, capacity, and urodynamics between porcine and human bladders, we envisage that our approach is also applicable to treating humans with UABs. In this regard, we provide the following considerations for its translation to humans.

First, we show that our MRB can be implanted in a minimally invasive manner to reduce surgical injury. Despite its large capacity (~300 ml), the soft nature of the entire MRB makes it possible to be compressed into a cylinder-like roll with a diameter and height of 4 and 12 cm, respectively (fig. S18). Therefore, a surgeon can place the MRB in the abdomen through a 4-cm-wide incision and complete the immobilization surgery by a laparoscope or other robotic systems, significantly minimizing the surgical injury. Second, the strong magnetic field of the cubic magnet, on one hand, is desired for actuating the MRB. On the other hand, it can also bring some inconvenience to our daily life. Therefore, a soft case with handles is specially designed to shield it from its surroundings (fig. S19, A and B). Also, we provide a detailed calculated and measured magnetic field strength around the cubic magnet (fig. S20 and tables S3 and S4) and define the safe distance when using the magnet (table S5). For example, for devices with high-quality magnetic cards, e.g., credit

cards, the recommended safe distance is >20 mm, while for implanted pacemakers and defibrillators, the safe distance is >60 mm. For portable devices such as smartphones and storage mediums, no damage is observed in our tests. Third, although our work moves forward a big step from prior works using mechanical compression to treat UAB, there is a long way before its fielded applications. We recommend performing urodynamics and electromyography before surgery to check the status of the detrusor and sphincter. According to the UAB classification scheme proposed by Madersbacher (*46*) (fig. S21), MRB is more suitable for patients with simple detrusor underactivity. For the patients with detrusor sphincter dyssynergia, our MRB can be combined with high-frequency alternating current (*47*) to block the pudendal nerve or implant an artificial sphincter (*48*) to achieve complete and controllable urination. For patients with mild to moderate UAB symptoms, conventional treatments are still highly recommended (table S1). Last but not least, we hope our work inspires more studies in this field. For instance, the actuation magnetic fields can be constructed by superposing a set of smaller magnets, and the actuation system may also be integrated into a home toilet for people in need (fig. S19C).

MATERIALS AND METHODS
Preparation of elastic magnetic composites
The silicone matrix was prepared using a silicone-based material, Ecoflex 00-30 (Smooth-on Inc.). For Ecoflex 00-30 components, the

volume ratio of part A and part B was 1:1, and it was then mixed up using a planetary mixer at 3000 rpm for 2 min.

The elastic magnetic composite was prepared by evenly mixing 25 and 40 weight % (wt %) of NdFeB microparticles (XINNUODE) having an average size of 5 μm with the uncured matrix composite size using a planetary mixer at 800 rpm for 2 min and then defoaming at 800 rpm for 1 min. An appropriate volume fraction of glossy (5 to 10 wt %) could be mixed in under the same conditions to adjust the fluid viscosity for the subsequent injection molding; this molding process should be completed within 30 min to avoid local curing of the silicone matrix or magnetic composite.

Characterization of magnetic composites
The magnetic moment densities of magnetic soft composites based on Ecoflex + NdFeB with different particle volume fraction were measured with a vibrating sample magnetometer (physical property measurement system, Quantum Design). Specimens were prepared from thin sheets of the composite materials obtained from molding by cutting them into circles with a diameter of 3 mm using a biopsy punch (Miltex Inc.) to fit into the sample holder of the magnetometer. The remnant magnetic moments of the samples were measured by the intercept between the magnetic moment loop curve and the positive y axis (magnetic moment) and then divided by the sample volume to obtain the magnetization or magnetic moment density.

Mechanical testing
Square planar sheets (40 mm by 40 mm by 1 mm) of magnetic soft composites based on Ecoflex embedded with different volume fractions of NdFeB microparticle were prepared by molding and then cut into dog bone–shaped specimens with known dimensions (width, 4 mm; gauge length, 25 mm) for tensile testing. The specimens were tested on a mechanical testing machine (Reger Inc., Shenzhen, China) with a deformation speed of 10 mm/min. A nominal stress-stretch curve was plotted for each specimen, and the shear modulus was determined by fitting the experimental curve to a neo-Hookean model.

Fabrication of MRB
The molds for MRB were fabricated with polylactic acid (PLA) using a 3D printer (A8, JGAURORA). First, the elastic magnetic composites were fabricated (fig. S6A), and the mesh for preconnection of different parts was cut into a specific shape. Then, the mesh was embedded into the elastic magnetic composites using Sil-Poxy (Smooth-On Inc.) before installation on the core (fig. S6B). The mesh for fixation was cut into 20-mm-wide and 300-mm-long ribbons in advance. Two sets of mesh were fixed on the upper and lower parting surfaces, respectively, while the extended mesh was clamped in the middle layer of the mold. The fabrication processes of matrix layers are described in detail in fig. S6D. The MRB was magnetized after removing excess Ecoflex by an impulse magnetic field (about 3.0 T) generated by a 180-mm-diameter impulse magnetizing coil with a power supply. This power supply was programmed to provide the magnetic polarities that define MRB's responsive motion.

Silicone gel skin formation
The uncoated samples were first cleaned with ethanol and isopropanol, followed by drying under nitrogen flow. The silica solution was prepared by mixing Ecoflex 00-30 (part A:part B = 1:1) and glossy in a 1:1 volume ratio using a centrifuge at 3000 rpm for 3 min. The prepared silica solution was loaded in a spray can and then evenly sprayed on the inside and outside surface of the samples using a spray gun with an air pump. The silica solution was gelatinized for 8 hours at 40°C, and then the prepared MRB was coated with a layer of silicone gel skin. The samples were then cleaned with ethanol and dried.

Hydrogel skin formation
Following the previously reported protocol (41), the uncoated MRB was first cleaned with ethanol and isopropanol, followed by drying under nitrogen flow. The dried MRB was then immersed in an organic solution of ethanol containing 10 wt % of benzophenone for 15 to 30 min. After rinsing with ethanol followed by drying under nitrogen flow, the samples were then immersed into a pre-gel solution containing 20 wt % of hydrogel monomers (acrylamide, Aladdin) and 1 wt % of Irgacure 2959 (Aladdin) in deionized water, which was degassed for 3 min before preparing the pre-gel solution. For ultraviolet (UV) curing, the pre-gel solution bath was subjected to UV irradiation (365-nm ultraviolet; CL-3000, Analytik Jena) for 60 min. Then, unreacted reagents were removed by rinsing with deionized water for 24 hours. The samples were analyzed using a Fourier transform infrared spectrophotometer (VERTEX 70 FTIR, Bruker) with a diamond crystal ATR (attenuated total reflectance) accessory. The spectra were obtained in the 4000 to 400 cm^{-1} region.

Friction coefficient measurement
Both coated and uncoated magnetic composites samples (20 mm by 20 mm by 1 mm) were prepared based on Ecoflex with 40 volume % 5-μm NdFeB microparticles. We measured the torque required to shear the specimens at prescribed shear rates of 1.0 s^{-1} under prescribed normal pressure (from 1 to 9 kPa) in normal force control mode by a 20-mm-diameter steel plate geometry from a rotational rheometer (AR-G2, TA Instruments). Deionized water was smeared on top of both hydrogel-coated and uncoated surfaces before shearing.

FE simulations
FE simulations were conducted by a commercial package Abaqus. To account for the interaction between magnetic composite with embedded hard magnetic particle and the external nonuniform magnetic field, we developed a user element (UEL) subroutine based on the continuum framework (49, 50). For a model of interest, we meshed it with a sufficiently large number of UEL (i.e., size of UEL is small enough) such that during each iteration of computation, the position-dependent magnetic field $\mathbf{B}$ and its gradient $\nabla\mathbf{B}$ at each element can be accurately calculated. Thereafter, the magnetic torque density $\boldsymbol{\tau}$ can be implemented by computing the magnetic Cauchy stress $\boldsymbol{\sigma}^{\mathbf{magnetic}} = -\mathbf{B} \otimes \mathbf{FM}$, where $\mathbf{F}$ is the deformation gradient and the operator $\otimes$ represents a dyadic product that takes two vectors to yield a second-order tensor, and magnetic body force in the current configuration can also be calculated as $\mathbf{f} = (\mathbf{FM}\cdot\nabla)\,\mathbf{B}$. Equilibrium is found by solving the equilibrium equation $\mathrm{div}(\boldsymbol{\sigma}^{\mathbf{elastic}} + \boldsymbol{\sigma}^{\mathbf{magnetic}}) + \mathbf{f} = 0$, where div represents the spatial divergence operation and $\boldsymbol{\sigma}^{\mathbf{elastic}}$ is the elastic Cauchy stress tensor. All simulations are checked with convergence.

The MRB is actuated by placing a cubic magnet with a width of 10 cm at a 2-cm distance away as depicted in Fig. 2B. The magnetic field around the cubic magnet can be analytically expressed according to Camacho and Sosa (51) and are plotted in Fig. 2 (C and D). Experimental measurements of the magnetization M and the density of the magnetic composite are presented in fig. S2 (A and C). Considering the symmetry of the structure, we built a 3D model by extruding the characteristic plane (i.e., XZ plane in Fig. 2B), where

black regions denote the magnetic composite and white areas represent the pure silicone.

The urination process was simulated in two steps: (i) initiating urination and (ii) voiding to empty. In the first step, the magnetic field is applied to increase the hydraulic pressure in the bladder. The volume of the MRB is set as a constant to simulate the incompressible behavior of the urine at the full state. This is realized by using a built-in function, Fluid Cavity, with incompressible fluid behavior in the interaction module in Abaqus. By moving the cubic magnet closer to the MRB (i.e., from negative z axis to positive z axis), the magnetic field around the MRB becomes stronger, yielding large magnetic torque τ and body force $\mathbf{f}$ to squeeze the MRB. Because of volume compressibility, the hydraulic pressure inside the MRB is increased. The maximum pressure increase ΔP inside the MRB is recorded when the distance between the magnet and the MRB reaches $D = 2$ cm. In the second step, the distance between the magnet and the MRB remained at 2 cm. To simulate the voiding behavior, the volume incompressibility constraint was removed and the pressure was gradually reduced to zero. The MRB further contracts to empty.

Ex vivo experiments
The ex vivo test setup is shown in fig. S7A. A mimic bladder with a thickness of 3 mm and a capacity of 250 ml was cast from silicone (Ecoflex 00-10) by 3D-printed mold as a substitute for pig's bladder. The outlet of the mimic bladder was connected to a differential pressure gauge and flow meter with hoses using a three-way valve. In the experiment, the bladder mimic full of water was wrapped in the MRB and then was pressed by the MRB under an applied magnetic field around a permanent magnet (length, width, and height: 100 mm). The permanent magnet gradually approached the MRB from below and then stopped at 20 mm from the lower surface of the MRB. The ex vivo tests of single urination lasted 60 to 90 s.

Ex vivo cytotoxicity analysis
Cell survival rate was tested on the HCV-29 cell line (human bladder epithelial cells, Otwo Biotech, China). HCV-29 cells were cultured in RPMI-1640 medium (Boster Biological Technology, Wuhan, China) supplemented with 10% fetal bovine serum (Gibco, Australia) and penicillin/streptomycin (Boster Biotechnology, Wuhan, China). To investigate the potential cytotoxicity of NdFeB and coating material, 10^4 cells per well were inoculated in 96-well plates and cultured for 24 hours at 37°C and 5% CO_2. These materials were cocultured with HCV-29 cells for 72 hours without changing the medium. Untreated cells and 70% ethanol-treated cells were used as positive and negative controls, respectively. After removing the cocultured material and replacing the medium, the cell survival rate was evaluated on the basis of a Cell Counting Kit-8 (CCK-8) assay according to the manufacturer's protocol (Boster Biotechnology, Wuhan, China) (34, 52). Briefly, 10 μl of CCK-8 reagent was added to each well and incubated for 1 hour at 37°C and 5% CO_2. The absorbance of each well was measured at 450 nm by a microplate reader (Multiskan FC, Thermo Fisher Scientific, USA). Cell survival was calculated by the following formula

$$\text{Cell survival rate (\%)} = (A_{\text{test}} - A_{\text{blank}}) \times 100\%$$

(Blank well: RPMI-1640 plus CCK-8 reagent).

Animal housing and physiological evaluation
All animal experiments were conducted by protocols approved by the Committee on Animal Care of Tongji Hospital, Huazhong University of Science and Technology (number: TJH-20191101). The characteristics of the bladders of female pigs are similar to those of humans, and the short urethra allows for facile catheterization and analysis of bladder function. The female Bama mini pigs (purchased from Hubei Yizhicheng Biotechnology Co. Ltd.) ranging from 6 to 9 months of age and weighing 25 to 35 kg were used in the in vivo tests. The animals were fed with food and water ad libitum in our animal facility and housed at a temperature of 22° ± 2°C and a relative humidity of 45 to 55% with a 12-hour light/12-hour dark cycle. Blood samples were taken from the right precaval vein with a disposable needle under sedation 1 day before operation and on POD 3, 7, and 14. Blood routine and blood biochemistry (including kidney function) were determined by an automated hematology analyzer (BC-2800Vet, Mindrey, China) and biochemistry analyzer (Chemray 800, Rayto Biotech, China). Urinary catheters (16 Fr, 20 ml, Cliny) were placed to take urine for subsequent urine tests (URIT-500B, URIT, China) 1 day before operation and on POD 3, 7, and 14. The behavioral assessment of the porcine was dependent on the Miami porcine walking scale (details are described in Supplementary Text) (53), which was applied by two trained investigators 1 day before operation and on POD 7 and 14.

Establishment of UAB porcine model
Sacral laminectomy and sacral nerve transection were performed to establish the UAB porcine model (32). Briefly, after anesthesia and preoperative routine preparation, a laminectomy was performed at the S2 to S5 vertebral level. Subsequently isolated skin, subcutaneous tissue, and fat were removed until the lateral erector spine muscles were fully exposed. All the muscles on the sacrum surface were separated below S1. The posterior sacrum wall was opened with a laminar rongeur, and then the residual sacrum with nucleus pulposus forceps was slowly removed to fully expose the cauda equina nerve and the accompanying bilateral S3 and S4 nerves. An electrical stimulation generator (3625 test stimulators, Medtronic, USA) was used to distinguish the ponytail and bilateral S1 to S5 nerves. The bilateral S2 and S3 nerves were separated with a nerve stripper, and the nerve was clamped with long-curved forceps; samples were taken after the bilateral S2 and S3 nerves were cut off. Muscle, subcutaneous tissue, and skin were sutured after hemostasis. Ceftiofur (5 mg/kg; Hysen Biotech, China) was intramuscularly injected 1 day before the operation and on POD 1, 2, and 3 to prevent infection. Animals were fasted 12 hours before the operation.

Magnetic resonance image
Magnetic resonance imaging (MRI) was conducted to obtain baseline data on sacral nerve morphology in pigs. Gadolinium-containing contrast agents were used to better display the sacral nerves. In our study, after anesthesia by Zoletil 50 [3 to 5 mg/kg, intramuscularly (i.m.)], we use a 3.0-T superconducting imager (GE, Signa HDx, USA) to analyze the morphology of normal sacral nerve. Pigs were covered with a quilt to keep warm during the inspection. MRI was performed again 24 hours after the operation to compare the changes of sacral nerves before and after surgery.

Implantation of MRB
Anesthesia and preoperative preparation were described above. Subsequently, a hernia repair mesh was used to fix the MRB outside the

bladder of a pig, referring to the surgical procedure for female pelvic organ prolapse (*44*). The pigs were placed in the supine position, and the skin, subcutaneous tissue, and fat were removed to expose the peritoneum (fig. S15A). The bladder was completely isolated (fig. S15B), and the MRB was fixed on the bladder (fig. S15C). The urethra was first fixed (fig. S15D), and the titanized polypropylene mesh attached to the sidewall of the MRB was pushed out of the skin from the inside out with a special hook (fig. S15F). When the lateral wall mesh was secured, the MRB was placed back in the original position of the bladder (fig. S15E). After placing a drainage tube in the abdominal cavity (fig. S15G), the abdomen was closed to complete the operation (fig. S15H).

Urodynamic tests

Urodynamic tests were also conducted to obtain baseline urination data urination 1 day before and 7 days after establishing the UAB model. After using Zoletil 50 for anesthesia (3 to 5 mg/kg, i.m.), a urodynamic tube (TDOC-7FD, Laborie, Canada) was connected to a urodynamic analysis machine (Andromeda, Germany) and inserted up to the bladder to measure bladder pressure (P_{ves}). An abdominal tube (TDOC-7FA, Laborie, Canada) was also inserted up to the rectum to evaluate abdominal pressure (P_{abd}). The detrusor pressure ΔP is calculated as $\Delta P = P_{ves} - P_{abd}$. Preheated normal saline was perfused at a rate of 50 ml/min. P_{ves} was continuously measured until urination occurred, and the maximum flow rate (Q_{max}) and maximum intravesical pressure were recorded. Each animal was measured at least three times. The urodynamic analysis was performed again 7 and 14 days after the MRB implantation.

H&E staining

Porcine kidney, ureter, and bladder tissue were isolated after the animals had been euthanized. The tissue was fixed in 10% formaldehyde, dehydrated with different graded ethanol, embedded in paraffin, and then sectioned (5 μm). The sections were dewaxed for 10 min and rehydrated in degraded ethanol (100, 95, 85, and 75%, respectively) for 5 min. After washing with distilled water for 1 min, the sections were stained with hematoxylin for 5 min. The sections were differentiated with 0.8 to 1% hydrochloric acid alcohol, followed by rinsing with tap water for 1 to 2 min. Then, the sections were dyed with eosin solution (alcohol-soluble) for 1 to 2 s and directly placed into anhydrous ethanol for dehydration for 1 to 2 min. H&E-stained sections were dipped in xylene and mounted with Histomount (Thermo Fisher Scientific) for microscopic examination (CX40, SOPTOP).

Immunohistochemistry

For immunohistochemistry, 5-μm porcine kidney, ureter, and bladder tissue sections were processed to assess local inflammation by evaluating the expression of IL-6. Sections were incubated with IL-6 (1:200; Bioss) primary antibodies at 37°C for 1 hour. Subsequently, the sections were incubated with goat anti-mouse IgG (Abcam, ab205719) as a biotinylated secondary antibody. Image-Pro Plus software (Media Cybernetics, Silver Spring, MD, USA) was used for semiquantitative analysis by testing the mean optical density.

Statistics

All analyses were carried out with GraphPad Prism (9.0, GraphPad Software, San Diego, CA, USA) and presented as means ± SDs. One-way analysis of variance (ANOVA) was used for the comparison of cytotoxicity analysis in vitro and physiological parameters in

animal experiments. Wilcoxon rank sum test was used for the comparison of the pathology scores between the two groups. Student's *t* test was used to compare the area of two groups in immunohistochemistry. $P < 0.05$ represents a statistical difference.

REFERENCES AND NOTES

1. Y. Aoki, H. W. Brown, L. Brubaker, J. N. Cornu, J. O. Daly, R. Cartwright, Urinary incontinence in women. *Nat. Rev. Dis. Primers.* **3**, 17042 (2017).
2. R. E. Hautmann, S. H. Hautmann, O. Hautmann, Complications associated with urinary diversion. *Nat. Rev. Urol.* **8**, 667–677 (2011).
3. W. Mahfouz, T. Al Afraa, L. Campeau, J. Corcos, Normal urodynamic parameters in women. *Int. Urogynecol. J.* **23**, 269–277 (2012).
4. J.-J. Wyndaele, Normality in urodynamics studied in healthy adults. *J. Urol.* **161**, 899–902 (1999).
5. A. D. Uren, N. Cotterill, C. Harding, C. Hillary, C. Chapple, M. Klaver, D. Bongaerts, Z. Hakimi, P. Abrams, Qualitative exploration of the patient experience of underactive bladder. *Eur. Urol.* **72**, 402–407 (2017).
6. N. I. Osman, C. R. Chapple, Contemporary concepts in the aetiopathogenesis of detrusor underactivity. *Nat. Rev. Urol.* **11**, 639–648 (2014).
7. R. Hamid, M. A. Averbeck, H. Chiang, A. Garcia, R. T. al Mousa, S. J. Oh, A. Patel, M. Plata, G. del Popolo, Epidemiology and pathophysiology of neurogenic bladder after spinal cord injury. *World J. Urol.* **36**, 1517–1527 (2018).
8. M. J. Drake, J. Williams, D. A. Bijos, Voiding dysfunction due to detrusor underactivity: An overview. *Nat. Rev. Urol.* **11**, 454–464 (2014).
9. O. Kalejaiye, M. J. Speakman, Management of acute and chronic retention in men. *Eur. Urol. Suppl.* **8**, 523–529 (2009).
10. N. I. Osman, C. R. Chapple, P. Abrams, R. Dmochowski, F. Haab, V. Nitti, H. Koelbl, P. van Kerrebroeck, A. J. Wein, Detrusor underactivity and the underactive bladder: A new clinical entity? A review of current terminology, definitions, epidemiology, aetiology, and diagnosis. *Eur. Urol.* **65**, 389–398 (2014).
11. M. H. D. Pfisterer, D. J. Griffiths, W. Schaefer, N. M. Resnick, The effect of age on lower urinary tract function: A study in women. *J. Am. Geriatr. Soc.* **54**, 405–412 (2006).
12. P. P. Smith, Aging and the underactive detrusor: A failure of activity or activation? *Neurourol. Urodyn.* **29**, 408–412 (2010).
13. M. M. Barendrecht, M. Oelke, M. P. Laguna, M. C. Michel, Is the use of parasympathomimetics for treating an underactive urinary bladder evidence-based? *BJU Int.* **99**, 749–752 (2007).
14. N. Hoag, J. Gani, Underactive bladder: Clinical features, urodynamic parameters, and treatment. *Int. Neurourol. J.* **19**, 185–189 (2015).
15. M. Miyazato, N. Yoshimura, M. B. Chancellor, The other bladder syndrome: Underactive bladder. *Rev. Urol.* **15**, 11–22 (2013).
16. N. I. Osman, F. Esperto, C. R. Chapple, Detrusor underactivity and the underactive bladder: A systematic review of preclinical and clinical studies. *Eur. Urol.* **74**, 633–643 (2018).
17. C. Gross, M. Habli, C. Lindsell, M. South, Sacral neuromodulation for nonobstructive urinary retention: A meta-analysis. *Female Pelvic Med. Reconstr. Surg.* **16**, 249–253 (2010).
18. A. M. Kajbafzadeh, L. Sharifi-Rad, S. S. Ladi-Seyedian, S. Mozafarpour, Transcutaneous interferential electrical stimulation for the management of non-neuropathic underactive bladder in children: A randomised clinical trial. *BJU Int.* **117**, 793–800 (2016).
19. G. Gakis, M. Ninkovic, G. A. van Koeveringe, S. Raina, G. Sturtz, M. S. Rahnama'i, K. D. Sievert, A. Stenzl, Functional detrusor myoplasty for bladder acontractility: Long-term results. *J. Urol.* **185**, 593–599 (2011).
20. E. K. Choi, C. H. Hong, M. J. Kim, Y. J. Im, H. J. Jung, S. W. Han, Effects of intravesical electrical stimulation therapy on urodynamic patterns for children with spina bifida: A 10-year experience. *J. Pediatr. Urol.* **9**, 798–803 (2013).
21. K. Radziszewski, Outcomes of electrical stimulation of the neurogenic bladder: Results of a two-year follow-up study. *NeuroRehabilitation* **32**, 867–873 (2013).
22. P. E. Levanovich, A. Diokno, D. L. Hasenau, M. Lajiness, R. Pruchnic, M. B. Chancellor, Intradetrusor injection of adult muscle-derived cells for the treatment of underactive bladder: Pilot study. *Int. Urol. Nephrol.* **47**, 465–467 (2015).
23. C. J. Fowler, D. Griffiths, W. C. de Groat, The neural control of micturition. *Nat. Rev. Neurosci.* **9**, 453–466 (2008).
24. R. D. Brierly, R. G. Hindley, E. McLarty, D. M. Harding, P. J. Thomas, A prospective controlled quantitative study of ultrastructural changes in the underactive detrusor. *J. Urol.* **169**, 1374–1378 (2003).

25. T. C. Chai, T. Kudze, New therapeutic directions to treat underactive bladder. *Investig. Clin. Urol.* **58**, S99–S106 (2017).

26. F. A. Hassani, W. Y. X. Peh, G. G. L. Gammad, R. P. Mogan, T. K. Ng, T. L. C. Kuo, L. G. Ng, P. Luu, S. C. Yen, C. Lee, A 3D printed implantable device for voiding the bladder using shape memory alloy (SMA) actuators. *Adv. Sci.* **4**, 1700143 (2017).

27. F. A. Hassani, G. G. L. Gammad, R. P. Mogan, T. K. Ng, T. L. C. Kuo, L. G. Ng, P. Luu, N. V. Thakor, S.-C. Yen, C. Lee, Design and anchorage dependence of shape memory alloy actuators on enhanced voiding of a bladder. *Adv. Mater. Technol.* **3**, 1700184 (2018).

28. F. Arab Hassani, R. P. Mogan, G. G. L. Gammad, H. Wang, S.-C. Yen, N. V. Thakor, C. Lee, Toward self-control systems for neurogenic underactive bladder: A triboelectric nanogenerator sensor integrated with a bistable micro-actuator. *ACS Nano* **12**, 3487–3501 (2018).

29. F. Arab Hassani, H. Jin, T. Yokota, T. Someya, N. V. Thakor, Soft sensors for a sensing-actuation system with high bladder voiding efficiency. *Sci. Adv.* **6**, eaba0412 (2020).

30. X. Yang, C. An, S. Liu, T. Cheng, V. Bunpetch, Y. Liu, S. Dong, S. Li, X. Zou, T. Li, H. Ouyang, Z. Wu, W. Yang, Soft artificial bladder detrusor. *Adv. Healthc. Mater.* **7**, e1701014 (2018).

31. S. Pane, T. Mazzocchi, V. Iacovacci, L. Ricotti, A. Menciassi, Smart implantable artificial bladder: An integrated design for organ replacement. *I.E.E.E. Trans. Biomed. Eng.* **68**, 2088–2097 (2021).

32. T. Guiho, C. Azevedo-Coste, D. Guiraud, C. Delleci, G. Capon, N. Delgado-Piccoli, L. Bauchet, J. R. Vignes, Validation of a methodology for neuro-urological and lumbosacral stimulation studies in domestic pigs: A humanlike animal model. *J. Neurosurg. Spine* **30**, 644–654 (2019).

33. G. Z. Lum, Z. Ye, X. Dong, H. Marvi, O. Erin, W. Hu, M. Sitti, Shape-programmable magnetic soft matter. *Proc. Natl. Acad. Sci. U.S.A.* **113**, E6007–E6015 (2016).

34. W. Hu, G. Z. Lum, M. Mastrangeli, M. Sitti, Small-scale soft-bodied robot with multimodal locomotion. *Nature* **554**, 81–85 (2018).

35. C. Zhou, Y. Yang, J. Wang, Q. Wu, Z. Gu, Y. Zhou, X. Liu, Y. Yang, H. Tang, Q. Ling, L. Wang, J. Zang, Ferromagnetic soft catheter robots for minimally invasive bioprinting. *Nat. Commun.* **12**, 5072 (2021).

36. Y. Kim, H. Yuk, R. Zhao, S. A. Chester, X. Zhao, Printing ferromagnetic domains for untethered fast-transforming soft materials. *Nature* **558**, 274–279 (2018).

37. R. Zhao, Y. Kim, S. A. Chester, P. Sharma, X. Zhao, Mechanics of hard-magnetic soft materials. *J. Mech. Phys. Solids* **124**, 244–263 (2019).

38. S. Wu, W. Hu, Q. Ze, M. Sitti, R. Zhao, Multifunctional magnetic soft composites: A review. *Multifunct. Mater.* **3**, 042003 (2020).

39. Y. Kim, X. Zhao, Magnetic soft materials and robots. *Chem. Rev.* **122**, 5317–5364 (2022).

40. S. H. Lee, D. Kim, M. Y. Baek, H. Tchah, Y. S. Kim, E. Ryoo, Y. M. Kim, Abdominal subcutaneous fat thickness measured by ultrasonography correlates with hyperlipidemia and steatohepatitis in obese children. *Pediatr. Gastroenterol. Hepatol. Nutr.* **18**, 108–114 (2015).

41. F. Köckerling, C. Schug-Pass, What do we know about titanized polypropylene meshes? An evidence-based review of the literature. *Hernia* **18**, 445–457 (2014).

42. Y. Yu, H. Yuk, G. A. Parada, Y. Wu, X. Liu, C. S. Nabzdyk, K. Youcef-Toumi, J. Zang, X. Zhao, Multifunctional "Hydrogel Skins" on diverse polymers with arbitrary shapes. *Adv. Mater.* **31**, 1807101 (2019).

43. Y. Kim, G. A. Parada, S. Liu, X. Zhao, Ferromagnetic soft continuum robots. *Sci. Robot.* **4**, eaax7329 (2019).

44. J. Liu, S. Qu, Z. Suo, W. Yang, Functional hydrogel coatings. *Natl. Sci. Rev.* **8**, nwaa254 (2020).

45. G. Campagna, L. Pedone Anchora, G. Panico, D. Caramazza, M. Arcieri, M. Cervigni, G. Scambia, A. Ercoli, Titanized polypropylene mesh in laparoscopic sacral colpopexy. *Int. Urogynecol. J.* **31**, 763–768 (2020).

46. H. Madersbacher, The various types of neurogenic bladder dysfunction: An update of current therapeutic concepts. *Paraplegia* **28**, 217–229 (1990).

47. A. Boger, N. Bhadra, K. J. Gustafson, Bladder voiding by combined high frequency electrical pudendal nerve block and sacral root stimulation. *Neurourol. Urodyn.* **27**, 435–439 (2008).

48. B. Peyronnet, G. Capon, O. Belas, A. Manunta, C. Allenet, J. Hascoet, J. Calves, M. Belas, P. Callerot, G. Robert, A. Descazeaud, G. Fournier, Robot-assisted AMS-800 artificial urinary sphincter bladder neck implantation in female patients with stress urinary incontinence. *Eur. Urol.* **75**, 169–175 (2019).

49. L. Wang, Y. Kim, C. F. Guo, X. Zhao, Hard-magnetic elastica. *J. Mech. Phys. Solids* **142**, 104045 (2020).

50. L. Wang, D. Zheng, P. Harker, A. B. Patel, C. F. Guo, X. Zhao, Evolutionary design of magnetic soft continuum robots. *Proc. Natl. Acad. Sci. U.S.A.* **118**, e2021922118 (2021).

51. J. M. Camacho, V. Sosa, Alternative method to calculate the magnetic field of permanent magnets with azimuthal symmetry. *Rev. Mex. Fis. E* **59**, 8–17 (2013).

52. D. Pan, K. Chen, Q. Zhou, J. Zhao, H. Xue, Y. Zhang, Y. Shen, Engineering of CdTe/SiO_2 nanocomposites: Enhanced signal amplification and biocompatibility for electrochemiluminescent immunoassay of alpha-fetoprotein. *Biosens. Bioelectron.* **131**, 178–184 (2019).

53. A. J. Santamaria, F. D. Benavides, K. R. Padgett, L. G. Guada, Y. Nunez-Gomez, J. P. Solano, J. D. Guest, Dichotomous locomotor recoveries are predicted by acute changes in segmental blood flow after thoracic spinal contusion injuries in pigs. *J. Neurotrauma* **36**, 1399–1415 (2019).